Measurement of π^{0} photoproduction on the proton at MAMI C

P. Adlarson *et al.* (A2 Collaboration at MAMI)

Phys. Rev. C **92**, 024617 — Published 24 August 2015

DOI: 10.1103/PhysRevC.92.024617

Measurement of π^0 photoproduction on the proton at MAMI C

P. Adlarson,[1] F. Afzal,[2] C. S. Akondi,[3] J. R. M. Annand,[4] H. J. Arends,[1] Ya. I. Azimov,[5] R. Beck,[2] N. Borisov,[6] A. Braghieri,[7] W. J. Briscoe,[8] S. Cherepnya,[9] F. Cividini,[1] C. Collicott,[10,11] S. Costanza,[7,12] A. Denig,[1] E. J. Downie,[1,8] M. Dieterle,[13] M. I. Ferretti Bondy,[1] L. V. Fil'kov,[9] A. Fix,[14] S. Gardner,[4] S. Garni,[13] D. I. Glazier,[4,15] D. Glowa,[15] W. Gradl,[1] G. Gurevich,[16] D. J. Hamilton,[4] D. Hornidge,[17] G. M. Huber,[18] A. Käser,[13] V. L. Kashevarov,[1,9] S. Kay,[15] I. Keshelashvili,[13] R. Kondratiev,[16] M. Korolija,[19] B. Krusche,[13] V. V. Kulikov,[20] A. Lazarev,[6] J. Linturi,[1] V. Lisin,[9] K. Livingston,[4] I. J. D. MacGregor,[4] D. M. Manley,[3] P. P. Martel,[1,21] M. Martemianov,[20] J. C. McGeorge,[4] W. Meyer,[22] D. G. Middleton,[1,17] R. Miskimen,[21] A. Mushkarenkov,[7,21] A. Neganov,[6] A. Neiser,[1] M. Oberle,[13] M. Ostrick,[1] P. Ott,[1] P. B. Otte,[1] B. Oussena,[1,8] D. Paudyal,[18] P. Pedroni,[7] A. Polonski,[16] V. V. Polyanski,[9] S. Prakhov,[1,8,23,*] A. Rajabi,[21] G. Reicherz,[22] G. Ron,[24] T. Rostomyan,[13] A. Sarty,[11] D. M. Schott,[8] S. Schumann,[1] C. Sfienti,[1] V. Sokhoyan,[1,8] K. Spieker,[2] O. Steffen,[1] I. I. Strakovsky,[8,†] Th. Strub,[13] I. Supek,[19] M. F. Taragin,[8] A. Thiel,[2] M. Thiel,[1] L. Tiator,[1] A. Thomas,[1] M. Unverzagt,[1] Yu. A. Usov,[6] S. Wagner,[1] D. P. Watts,[15] D. Werthmüller,[4,13] J. Wettig,[1] L. Witthauer,[13] M. Wolfes,[1] R. L. Workman,[8] and L. A. Zana[15]

(A2 Collaboration at MAMI)

[1] *Institut für Kernphysik, University of Mainz, D-55099 Mainz,Germany*
[2] *Helmholtz-Institut für Strahlen- und Kernphysik, University of Bonn, D-53115 Bonn, Germany*
[3] *Kent State University, Kent, Ohio 44242-0001, USA*
[4] *SUPA School of Physics and Astronomy, University of Glasgow, Glasgow G12 8QQ, United Kingdom*
[5] *Petersburg Nuclear Physics Institute, 188300 Gatchina, Russia*
[6] *Joint Institute for Nuclear Research, 141980 Dubna, Russia*
[7] *INFN Sezione di Pavia, I-27100 Pavia, Italy*
[8] *The George Washington University, Washington, DC 20052-0001, USA*
[9] *Lebedev Physical Institute, 119991 Moscow, Russia*
[10] *Dalhousie University, Halifax, Nova Scotia B3H 4R2, Canada*
[11] *Saint Mary's University, Halifax, Nova Scotia B3H 3C3, Canada*
[12] *Dipartimento di Fisica, Università di Pavia, I-27100 Pavia, Italy*
[13] *Institut für Physik, University of Basel, CH-4056 Basel, Switzerland*
[14] *Laboratory of Mathematical Physics, Tomsk Polytechnic University, 634034 Tomsk, Russia*
[15] *School of Physics, University of Edinburgh, Edinburgh EH9 3JZ, United Kingdom*
[16] *Institute for Nuclear Research, 125047 Moscow, Russia*
[17] *Mount Allison University, Sackville, New Brunswick E4L 1E6, Canada*
[18] *University of Regina, Regina, Saskatchewan S4S 0A2, Canada*
[19] *Rudjer Boskovic Institute, HR-10000 Zagreb, Croatia*
[20] *Institute for Theoretical and Experimental Physics, SRC Kurchatov Institute, Moscow, 117218 Russia*
[21] *University of Massachusetts, Amherst, Massachusetts 01003, USA*
[22] *Institut für Experimentalphysik, Ruhr-Universität, D-44780 Bochum, Germany*
[23] *University of California Los Angeles, Los Angeles, California 90095-1547, USA*
[24] *Racah Institute of Physics, Hebrew University of Jerusalem, Jerusalem 91904, Israel*

Differential cross sections for the $\gamma p \to \pi^0 p$ reaction have been measured with the A2 tagged-photon facilities at the Mainz Microtron, MAMI C, up to the center-of-mass energy $W = 1.9$ GeV. The new results, obtained with a fine energy and angular binning, increase the existing quantity of π^0 photoproduction data by $\sim 47\%$. Owing to the unprecedented statistical accuracy and the full angular coverage, the results are sensitive to high partial-wave amplitudes. This is demonstrated by the decomposition of the differential cross sections in terms of Legendre polynomials and by further comparison to model predictions. A new solution of the SAID partial-wave analysis obtained after adding the new data into the fit is presented.

PACS numbers: 12.38.Aw,13.60.Rj,14.20.-c,25.20.Lj

I. INTRODUCTION

Measurements of pion photoproduction on both proton and quasifree-neutron targets have a very long history, started about 65 years ago. Using the first bremsstrahlung facilities, pioneering results for $\gamma p \to \pi^0 p$ [1], $\gamma p \to \pi^+ n$ [2], and $\gamma n \to \pi^- p$ [3] were obtained. Despite all the shortcomings of the first measure-

*corresponding author, e-mail: prakhov@ucla.edu
†corresponding author, e-mail: igor@gwu.edu

ments (such as large normalization uncertainties, wide energy and angular binning, limited angular coverage, etc.), those data were crucial for the discovery of the first excited nucleon state, $\Delta(1232)3/2^+$ [4].

Though present electromagnetic facilities in combination with modern experimental detectors have allowed a significant improvement in the quantity and quality of pion-photoproduction data [5], full understanding of pion-photoproduction dynamics is far from established, even in the best investigated area, comprising the first, second, and third resonance regions. The properties of many nucleon states in this energy range, especially in the third resonance region [6], are still not well understood. Resolving the complex partial-wave structure of pion photoproduction with minimal model assumptions requires more precise data for differential cross sections, with fine energy binning and full angular coverage, in combination with measurements of various polarization observables.

First results for polarization degrees of freedom have been recently reported by the A2, CBELSA/TAPS, and GRAAL Collaborations. The beam asymmetry Σ has been measured by GRAAL [7] and CBELSA/TAPS [8]. Data for the other two single polarization observables T (target polarization) and P (recoil-nucleon polarization measured as a double-polarization observable with transversely polarized target and linearly polarized beam) have been reported from CBELSA/TAPS [9]. First results for double-polarization asymmetries have also been measured at CBELSA/TAPS with a longitudinally polarized target (observable G with linearly polarized beam [8] and observable E with circularly polarized beam [10]) and with a transversely polarized target and linearly polarized beam (observable H [9]). The A2 Collaboration at MAMI obtained results for the double-polarization asymmetry $C_x^\star$ using a circularly polarized photon beam and a nucleon recoil polarimeter [11]. Further data sets are currently under analysis, so that one can expect new analyses which provide much tighter constraints on the $\gamma p \to \pi^0 p$ reaction in the nearest future.

This work contributes to these efforts by presenting a new high-statistics measurement of the $\gamma p \to \pi^0 p$ differential cross sections conducted by the A2 Collaboration for incident-photon energies, E_γ, from 218 MeV up to 1573 MeV [or center-of-mass (c.m.) energies $W = 1136 - 1957$ MeV]. The data are obtained with a fine binning in E_γ ($\sim$ 4 MeV for all energies below $E_\gamma = 1120$ MeV) and 30 angular bins, covering the full range of the π^0 production angle. The data obtained above $E_\gamma = 1443$ MeV ($W = 1894$ MeV) have limited angular coverage.

A more detailed analysis of the present $\gamma p \to \pi^0 p$ differential cross sections, combined with results from the A2 Collaboration obtained by measuring polarization observables, is currently in progress and will be published separately.

II. EXPERIMENTAL SETUP

The reaction $\gamma p \to \pi^0 p$ was measured using the Crystal Ball (CB) [12] as a central calorimeter and TAPS [13, 14] as a forward calorimeter. These detectors were installed at the energy-tagged bremsstrahlung-photon beam produced from the electron beam of the Mainz Microtron (MAMI) [15, 16].

The CB detector is a sphere consisting of 672 optically isolated NaI(Tl) crystals, shaped as truncated triangular pyramids, which point toward the center of the sphere. The crystals are arranged in two hemispheres that cover 93% of 4π sr, sitting outside a central spherical cavity with a radius of 25 cm, which is designed to hold the target and inner detectors.

In the A2 experiments at MAMI C, TAPS was initially arranged in a plane consisting of 384 BaF_2 counters of hexagonal cross section. It was installed 1.5 m downstream of the CB center and covered the full azimuthal range for polar angles from 1° to 20°. In the present experiments, 18 BaF_2 crystals, covering polar angles from 1° to 5°, were replaced with 72 $PbWO_4$ crystals. This allowed running with a much higher MAMI electron current, without decreasing the TAPS efficiency due to the very high count rate in the crystals near the photon-beam line. The energy resolution of the $PbWO_4$ crystals has not been understood well yet, and the use of their information was restricted in the present analysis, as described later. More details on the calorimeters and their resolutions are given in Ref. [17] and references therein.

The present measurements used 1557-MeV and 1604-MeV electron beams from the Mainz Microtron, MAMI C [16]. The data with the 1557-MeV beam were taken in the first half of 2013 (Run-I) and those with the 1604-MeV beam in the second half of 2014 (Run-II). Bremsstrahlung photons, produced by the beam electrons in a 10-μm Cu radiator and collimated by a 4-mm-diameter Pb collimator, were incident on a 10-cm-long liquid hydrogen (LH_2) target located in the center of the CB. In Run-I with the 1557-MeV electron beam, the energies of the incident photons were analyzed up to 1448 MeV by detecting the postbremsstrahlung electrons in the Glasgow tagged-photon spectrometer (Glasgow tagger) [18–20]. The uncertainty in the energy of the tagged photons is mainly determined by the number of tagger focal-plane detectors in combination with the energy of the MAMI electron beam used in the experiments. Increasing the MAMI energy results in increasing both the energy range covered by the spectrometer and the corresponding uncertainty in E_γ. For the MAMI energy of 1557 MeV and the Glasgow tagger, such an uncertainty was about ± 2 MeV. The systematic uncertainty in the absolute value of E_γ, which is dominated by the energy calibration of the tagger, was about 0.5 MeV [20]. More details on the tagger energy calibration and uncertainties in the energies can be found in Ref. [21].

In Run-II with the 1604-MeV electron beam, the energies of the incident photons were analyzed from 1426 MeV up to 1576 MeV by detecting the post-

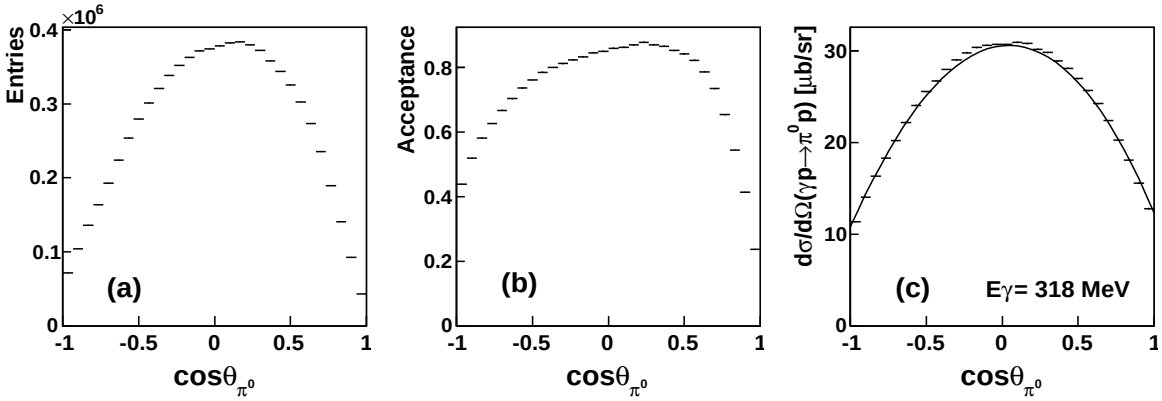

FIG. 1: $\cos\theta$ distributions for $\gamma p \to \pi^0 p$, with θ being the angle between the directions of the outgoing π^0 and the incident photon in the c.m. frame, obtained for $E_\gamma = 318$ MeV (W=1215 MeV): (a) experimental data after subtraction of the empty-target and the random background; (b) angular acceptance obtained from the MC simulation of $\gamma p \to \pi^0 p$; (c) results for the $\gamma p \to \pi^0 p$ differential cross section compared to the prediction by SAID [23] with its CM12 [24] solution. The error bars on all data points represent statistical uncertainties only.

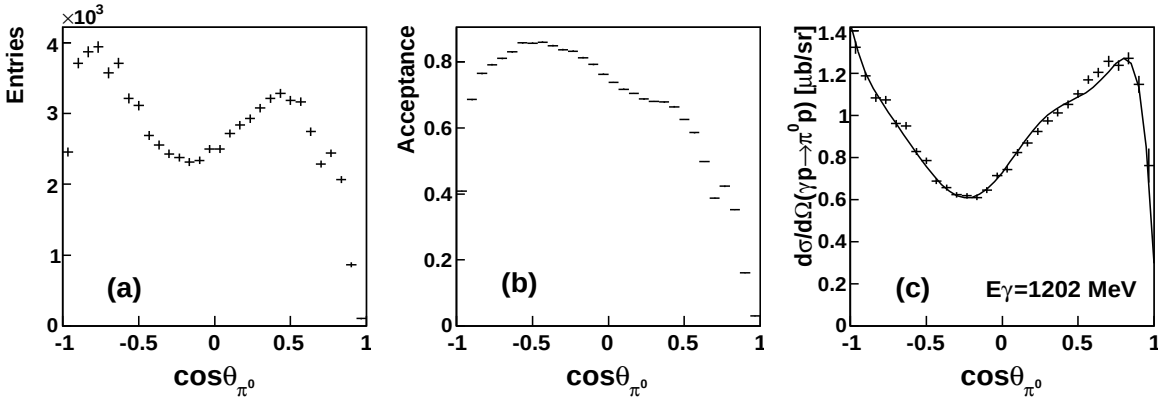

FIG. 2: Same as Fig. 1, but for $E_\gamma = 1202$ MeV (W=1771 MeV).

bremsstrahlung electrons in the Mainz end-point tagger (EPT) with 47 focal-plane detectors. Since the Glasgow tagger was not designed to measure the high-energy tail of the bremsstrahlung spectrum, the EPT spectrometer was built to conduct η' measurements by covering this low-energy range of postbremsstrahlung electrons. The uncertainty of the EPT in E_γ due to the width of its focal-plane detectors was about ± 1.6 MeV, with a similar value (i.e. ~ 1.6 MeV) in the systematic uncertainty in E_γ due to the EPT energy calibration. The energy calibration of the EPT is based only on the simulation of electron tracing, using measured magnetic-field maps. The correctness of this calibration, as well as its uncertainty, was checked by measuring the position of the η' threshold, $E_\gamma \approx 1447$ MeV.

Because the main goal of Run-I was to measure the $\gamma p \to \pi^0 p$ reaction from $E_\gamma = 218$ MeV up to 1448 MeV and with full coverage of the π^0 production angle, the trigger required the total energy deposited in the CB to exceed $\sim$120 MeV. Run-II was mainly dedicated to studying η' physics. For that, the experimental trigger required the CB energy to exceed $\sim$540 MeV, rejecting the detection of π^0 production in the very forward and backward angles.

III. DATA HANDLING

The reaction $\gamma p \to \pi^0 p \to \gamma\gamma p$ was searched for in events reconstructed with two or three clusters detected in the CB and TAPS together. In the analysis of the data from Run-I, the information from the 72 $PbWO_4$ crystals of TAPS was not used at all. In the analysis of the data from Run-II, in which all $PbWO_4$ crystals demostrated good performance, their information was used in the cluster reconstruction. The two-cluster events were analyzed assuming that the final-state proton was not detected. This typically happens when the outgoing proton is stopped in the material of the downstream beam tunnel of the CB, or the proton kinetic energy in the lab system is below the software cluster threshold, which was 12 MeV in the present analysis.

The selection of event candidates and the reconstruction of the reaction kinematics were based on the kinematic-fit technique. Details on the kinematic-fit parameterization of the detector information and resolutions are given in Ref. [17]. The kinematic-fit technique was also used for the offline calibration of the calorimeters. The resolution functions used in the kinematic fit were adjusted to result in proper stretch functions (or

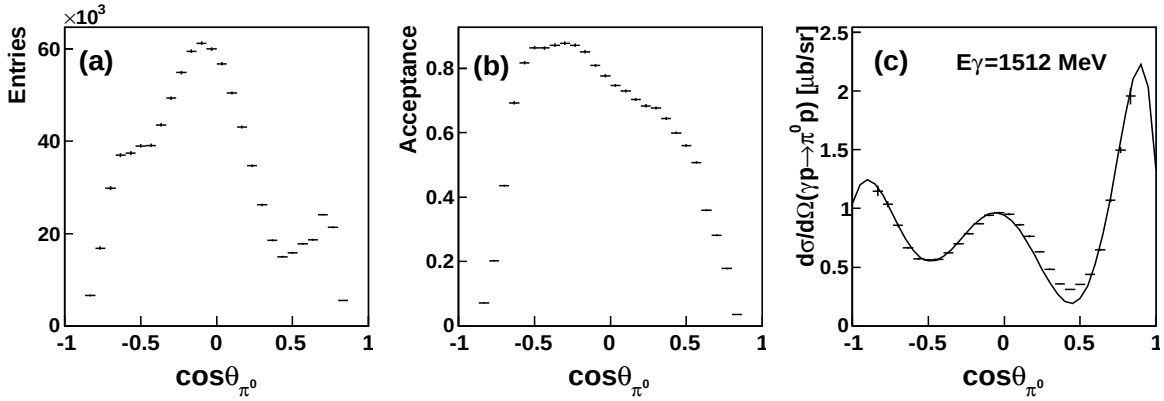

FIG. 3: Same as Fig. 1, but for $E_\gamma = 1512$ MeV (W=1928 MeV).

pulls) and probability distributions. All two- and three-cluster events that satisfied the $\gamma p \to \pi^0 p \to \gamma\gamma p$ hypothesis with a probability greater than 1% were accepted for further analysis. The kinematic-fit output was used to reconstruct the four-momenta of the outgoing particles. The events from the data of Run-II with more than one cluster in the 72 $PbWO_4$ crystals of TAPS were discarded from the analysis, and the events with one cluster in these crystals were tested only for the hypothesis assuming that this cluster is produced by the recoil proton. Such a restriction was imposed due to the unknown energy-resolution function for the $PbWO_4$ crystals, and only the angular information from the proton cluster was used in the kinematic fit.

The determination of the experimental acceptance was based on a Monte Carlo (MC) simulation of $\gamma p \to \pi^0 p \to \gamma\gamma p$ with an isotropic production-angular distribution and a uniform beam distribution generated for the full energy range of the tagged bremsstrahlung photons. All MC events were propagated through a GEANT (3.21) simulation of the experimental setup. To reproduce the experimental resolutions, the GEANT output was subject to additional smearing, thus allowing both the simulated and experimental data to be analyzed in the same way. This additional smearing was adjusted by describing the experimental invariant-mass resolutions as well as the kinematic-fit probability distributions. The final adjustment of the detection efficiency for $\gamma p \to \pi^0 p \to \gamma\gamma p$ took into account the trigger requirements in the analysis of the MC events.

MC simulations for other possible reactions (such as $\gamma p \to \eta p \to \gamma\gamma p$, $\gamma p \to \pi^0\pi^0 p$, $\gamma p \to \omega p \to \pi^0\gamma p$, $\gamma p \to \pi^0\pi^+ n$) showed that background contributions from these sources were negligibly small. Thus, experimental spectra with selected events were contaminated only by two sources of background events, the distributions of which were directly subtracted afterwards. The first source of background was due to interactions of incident photons in the windows of the target cell. The subtraction of this background was based on the analysis of data samples that were taken with an empty (no liquid hydrogen) target. The weight for the subtraction of the empty-target spectra was taken as a ratio of the photon-beam fluxes for the data samples with the full and the empty target. A second background was caused by random coincidences of the tagger counts with the experimental trigger; its subtraction was carried out by using event samples for which all coincidences were random (see Refs. [17, 22] for more details).

For measuring the $\gamma p \to \pi^0 p$ differential cross sections, all selected events were divided into 30 equal-width $\cos\theta$ bins, covering the full range from -1 to 1, where θ is the angle between the directions of the outgoing π^0 and the incident photon in the c.m. frame. Also, the quantity of data collected for $\gamma p \to \pi^0 p$ was sufficient to obtain statistically accurate differential cross sections for every tagger channel in the energy range from $E_\gamma = 218$ MeV to 1120 MeV, providing ~ 4 MeV binning in E_γ. For higher energies, energy bins were combined in two or more tagger channels.

The typical experimental statistics and acceptance are illustrated in Figs. 1, 2, and 3 for different energies and data sets. Figure 1(a) shows the experimental $\cos\theta$ distribution for $E_\gamma = 318$ MeV (W=1215 MeV), which is obtained after subtracting the random and the empty-target backgrounds. Since this energy bin is close to the $\Delta(1232)3/2^+$ maximum, the statistical uncertainties in this distribution, based on 8×10^6 events, are very small ($\sim 0.2\%$). Figure 1(b) shows the corresponding angular acceptance, which is greater than 80% for the central range of π^0 production angles. The resulting $\gamma p \to \pi^0 p$ differential cross section for $E_\gamma = 318$ MeV is depicted in Fig. 1(c). It is also compared to the prediction from the partial-wave analysis (PWA) by SAID [23] with its CM12 [24] solution (shown by a solid line). The experimental data points lie slightly above the phenomenological prediction, but their angular dependence is very close to it. Because all modern PWAs give very similar predictions for the $\gamma p \to \pi^0 p$ differential cross section at the $\Delta(1232)3/2^+$ maximum, the present results in this region do not contradict any of them.

Figure 2(a) shows the experimental $\cos\theta$ distribution for $E_\gamma = 1202$ MeV (W=1771 MeV), which is near the third resonance region. The statistical uncertainties in this distribution, based on 8.5×10^4 events, are larger but are still sufficient for a reliable analysis of the resulting

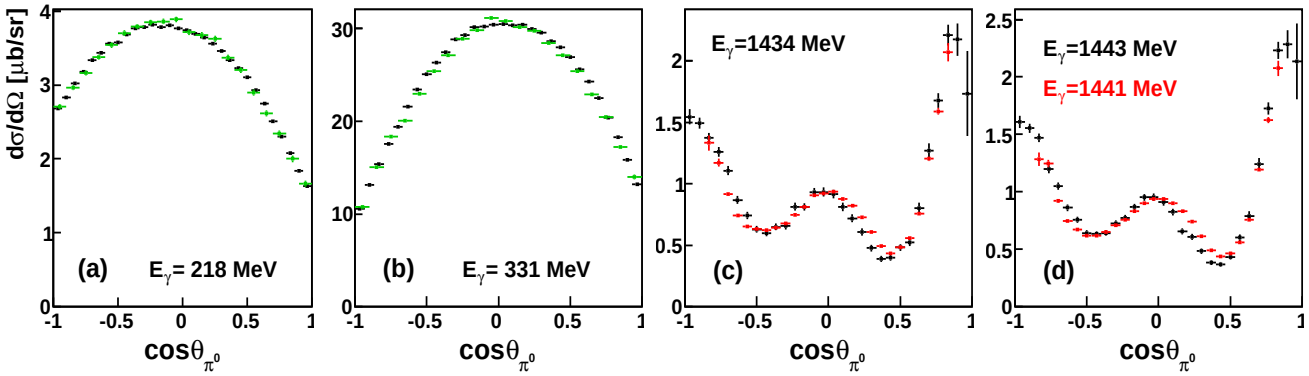

FIG. 4: (Color online) Comparison of the $\gamma p \to \pi^0 p$ differential cross sections obtained by the A2 Collaboration in different experiments: (a) results for $E_\gamma = 218$ MeV from Run-I (black points) and from the experiment [25] with MAMI energy of 855 MeV (green points); (b) same as (a) but for $E_\gamma = 331$ MeV; (c) results for $E_\gamma = 1434$ MeV from Run-I (black points) and Run-II (red points); (d) same as (c) but for $E_\gamma = 1443$ and 1441 MeV of Run-I and Run-II, respectively; The error bars on all data points represent statistical uncertainties only.

differential cross section. Since the shape of the $\gamma p \to \pi^0 p$ differential cross sections in this region changes rapidly with energy, the main goal of the present work was to measure it with the finest energy binning. Figure 2(b) shows that the angular acceptance drops for the very forward angles. At these energies, this occurs as many π^0 mesons produced at forward angles have both their decay photons going into TAPS, and such events do not pass the trigger requirements. The resulting differential cross section, plotted in Fig. 2(c), demonstrates again a quite reasonable agreement with the SAID CM12 solution [24].

Figure 3 shows the $\cos\theta$ distributions for $E_\gamma = 1512$ MeV (W=1928 MeV) from the data taken in Run-II. Despite the large quantity of the experimental events (9×10^5), a very low, and even zero, acceptance for the very forward and backward angles, caused by the trigger, did not allow the first two and the last two $\cos\theta$ bins to be measured. However, the remaining 26 data points of the differential cross section lie close to the prediction from SAID CM12 [24].

IV. EXPERIMENTAL RESULTS AND THEIR DISCUSSION

The $\gamma p \to \pi^0 p$ differential cross sections were obtained by taking into account the number of protons in the LH_2 target and the photon-beam flux from the tagging facilities corrected for the fraction rejected by collimators. The overall systematic uncertainty due to the calculation of the detection efficiency and the photon-beam flux was estimated to be 4% for the data taken in Run-I and 5% for the data taken in Run-II.

Another source of systematic uncertainty is due to imperfections in reproducing the angular dependence of the $\cos\theta$ acceptance. Such imperfections are easier to see in differential cross sections with very low statistical uncertainties and a smooth shape. In the present data, it can be seen, for example, on the top of the experimental spectrum shown in Fig. 1(c). The angular dependence of differential cross sections can also be smeared due to the limited resolution in the π^0 production angle, resulting in a larger population of angular bins with a lower cross section. Such an effect is, possibly, seen in Fig. 3(c) near $\cos\theta = 0.5$.

Possible magnitudes of systematic uncertainties in differential cross sections can be checked by comparing similar results obtained by analyzing different data. Figure 4 illustrates self-consistency of the results for the $\gamma p \to \pi^0 p$ differential cross sections obtained by the A2 Collaboration in three different experiments. The results for the lowest energy, $E_\gamma = 218$ MeV, taken in Run-I are compared in Fig. 4(a) with similar results obtained in the A2 experiment (A2-2008) with the Glasgow tagger and MAMI energy of 855 MeV [25]. As seen, the agreement of the two independent measurements is fairly good for both the absolute values and the angular dependence. Figure 4(b) compares the results of Run-I and A2-2008 for an energy near the $\Delta(1232)3/2^+$ maximum, showing a small discrepancy in the angular dependence. Continuing the comparison of the results from Run-I and A2-2008 at energies above the $\Delta(1232)3/2^+$ peak makes little sense as, at those energies, the A2-2008 data have much larger systematic uncertainties in the photon flux and in the angular acceptance, affected by the trigger. The results for two the highest energies, $E_\gamma = 1434$ and 1443 MeV, taken in Run-I are compared in Figs. 4(c) and (d) with similar results from the present work obtained in Run-II. Despite a general agreement, there are some discrepancies between the two sets of results, which cannot be explained by their statistical uncertainties. In our opinion, such discrepancies could be caused by several factors. There was a significant difference in the trigger of the two experiments and in the energy resolution of the calorimeters, as the experiment with the EPT (Run-II) was made with a much higher MAMI electron current. A poorer energy resolution in Run-II resulted in a larger smearing of the $\cos\theta$ angular dependence. Another possible explana-

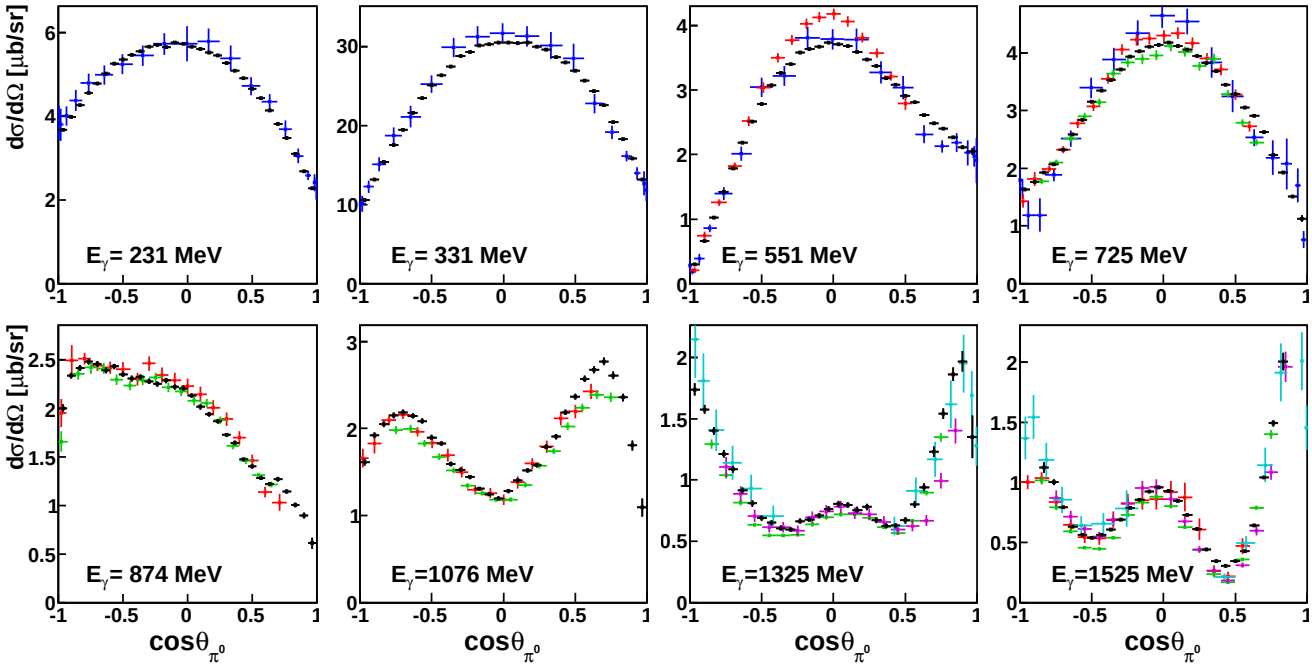

FIG. 5: (Color online) Comparison of the $\gamma p \to \pi^0 p$ differential cross sections from the present work (black points) with most recent results from other experimental setups at MAMI [26] (blue points) and other facilities: GRAAL [7] (red points), CLAS [27] (green points), CB-ELSA [28] (magenta points), and CBELSA/TAPS [29] (cyan points). Values of E_γ in each panel indicate the photon-beam energies for the results of this work. All data from other experiments are shown for nearby energies. The error bars on the data points from this work represent statistical uncertainties only. The uncertainties of some previous results also include angular-dependent systematic uncertainties.

tion is a slight mismatch in the energy calibrations of the two different tagged-photon spectrometers. Overall, the average systematic uncertainty in the differential cross sections due to the resolution in the c.m. θ and possible imperfections in the angular acceptance was estimated to be 2% for the results of Run-I. The corresponding systematic uncertainty for the results of Run-II is at least twice as high.

Comparison of the results for the $\gamma p \to \pi^0 p$ differential cross sections from the present work with the most recent published data from other collaborations [7, 26–29] is illustrated in Fig. 5 for eight different energies. Previous results with either large angular bins or very restricted angular coverage are not included in the comparison. As seen in Fig. 5, data with full angular coverage existed only in the region below the third resonance region. The results of this work are in a general agreement with all the data shown, although those data are not always entirely consistent with each other. As also evident, the present data from Run-I have much superior statistical accuracy, combined with a finer angular and energy binning.

The total cross sections for $\gamma p \to \pi^0 p$ were determined by integrating the differential cross sections for the data obtained from Run-I, which have the full angular coverage. The resulting total cross sections are plotted in Fig. 6 as a function of the c.m. energy W along with earlier A2 results obtained for energies up to $E_\gamma = 444$ MeV (W=1309 MeV) [25] and results from Ref. [26], obtained for energies up to $E_\gamma = 790$ MeV (W=1537 MeV), and from Ref. [28], obtained for energies above $E_\gamma = 300$ MeV (W=1201 MeV). The latter data have no full angular coverage; they were obtained with extrapolating experimental differential cross sections into forward and backward angles by using the corresponding PWA results. For completeness, the data at higher energies are also compared in Fig. 6(b) to the SAID solution CM12 [24], shown by a magenta dashed line. As seen in Fig. 6(a) and (b), the present results are in good agreement, within the total uncertainties (calculated by adding the statistical and the overall systematic uncertainty in quadrature), with the earlier A2 results and in general agreement with the most recent experimental data and SAID CM2 solution based on fitting previous data, even if they do not have the full angular coverage.

Comparison of the present results for the $\gamma p \to \pi^0 p$ differential cross sections with predictions of different partial-wave and coupled-channel analyses is illustrated for selected energies in Fig. 7. Three sets of predictions shown in this figure correspond to PWAs (namely, SAID CM12 [24], MAID2007 [30], and Bonn-Gatchina BG2014-02 [31]) based on fitting previous data. The fourth set of curves comes from SAID PR15 solution obtained after adding the present data points into the SAID fit. Compared to the SAID solution CM12, the new fit PR15 also involves the data added to obtain SAID DU13 solution [5] and other most recent polarization data from CBELSA/TAPS [9, 10] and A2 at MAMI [11]. As seen, all three the previous PWAs are very close to each

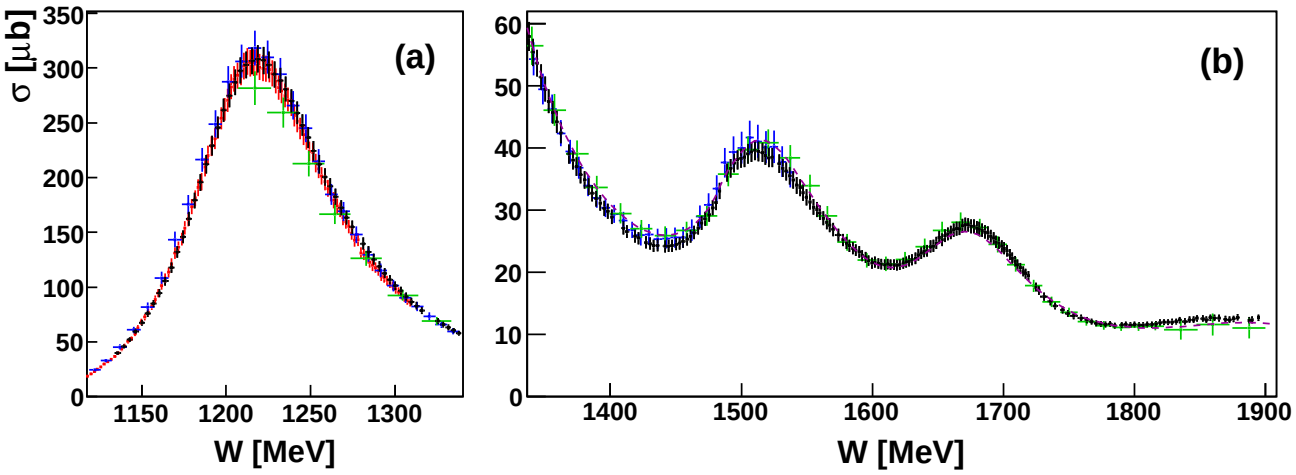

FIG. 6: (Color online) Total cross sections for $\gamma p \to \pi^0 p$ from this work (black points) as a function of the c.m. energy W compared with earlier A2 results [25] (red points), with results from Ref. [26] (blue points) and Ref. [28] (green points), and with the SAID solution CM12 [24] shown in panel (b) by a magenta dashed line. For a better comparison, the energy range is divided in two intervals: (a) $W < 1340$ MeV and (b) $W > 1340$ MeV. The error bars on the experimental data points represent their total uncertainties.

TABLE I: Average χ^2/dp values (including information on the total χ^2 from Eq. (1) and the number of data points used) for MAID2007 [30] (fitting data only below $W = 2$ GeV) and three SAID solutions: CM12 [24], DU13 [5], and PR15.

χ^2/dp	MAID2007	SAID CM12	SAID DU13	SAID PR15
present $\gamma p \to \pi^0 p$	99722/7978 = 12.5	24036/7978 = 3.0	28745/7978 = 3.6	9434/7978 = 1.2
previous				
$\gamma p \to \pi^0 p$	135195/15468 = 8.7	73211/17087 = 4.3	41500/17087 = 2.4	40793/17087 = 2.4
$\gamma p \to \pi^+ n$	171853/8092 = 21.2	23533/8959 = 2.6	19312/8959 = 2.2	17540/8959 = 2.0
$\gamma n \to \pi^- p$	25335/2806 = 9.0	53657/3162 = 17.0	7561/3162 = 2.4	6572/3162 = 2.1
$\gamma n \to \pi^0 n$	22568/364 = 62.0	979/364 = 2.7	1436/364 = 4.0	1187/364 = 3.3

other and to the present data points in the energy region around the $\Delta(1232)3/2^+$ maximum. Differences between the PWAs themselves as well as between the PWAs and the data points increase, especially for the MAID2007 solution, at energies that are away from the $\Delta(1232)3/2^+$ peak. Then all the PWAs and the data points become closer again in the second and the third resonance regions. The largest difference between the present data and the three previous PWAs is observed for the MAID2007 solution; this could be explained by the fact that many of the most recent data sets were not available at the time when the MAID2007 solution was released.

Quantitatively, the agreement of the present data with PWAs can usually be estimated via χ^2 values calculated from deviations of experimental data points from PWA solutions. The χ^2 function used in the minimization procedure by SAID is given by formula [32]

$$\chi^2 = \sum_i \left(\frac{X\Theta_i - \Theta_i^{\rm exp}}{\epsilon_i}\right)^2 + \left(\frac{X-1}{\epsilon_X}\right)^2, \qquad (1)$$

where $\Theta_i^{\rm exp}$ is an individual experimental value of the differential cross section with its uncertainty ϵ_i (includes both the statistical and the individual systematic uncertainty discussed in the text above), Θ_i is the fit value calculated for the same energy and the production angle, and X is a normalization parameter with its uncertainty ϵ_X that is determined by the overall systematic uncertainties of the data (see start of this section). The average χ^2/dp values, along with the information on the total χ^2 from Eq. (1) and the number of data points used (dp), are listed in Table I for MAID2007 [30] and three SAID solutions: CM12 [24], DU13 [5], and PR15. As seen, the numbers in Table I confirm that the average χ^2/dp is worse for the older solution MAID2007 than for the more recent SAID solutions CM12 and DU13. The magnitudes of χ^2/dp obtained for the new SAID solution PR15 indicate that the new $\gamma p \to \pi^0 p$ data are consistent with the existing $\gamma N \to \pi N$ data sets. The number of data points available for each photoproduction reaction, which are listed in Table I, shows that the present $\gamma p \to \pi^0 p$ data increase the existing $\gamma p \to \pi^0 p$ statistics by $\sim 47\%$ and the existing $\gamma N \to \pi N$ statistics by $\sim 27\%$.

The χ^2/dp values, averaged within each energy bin,

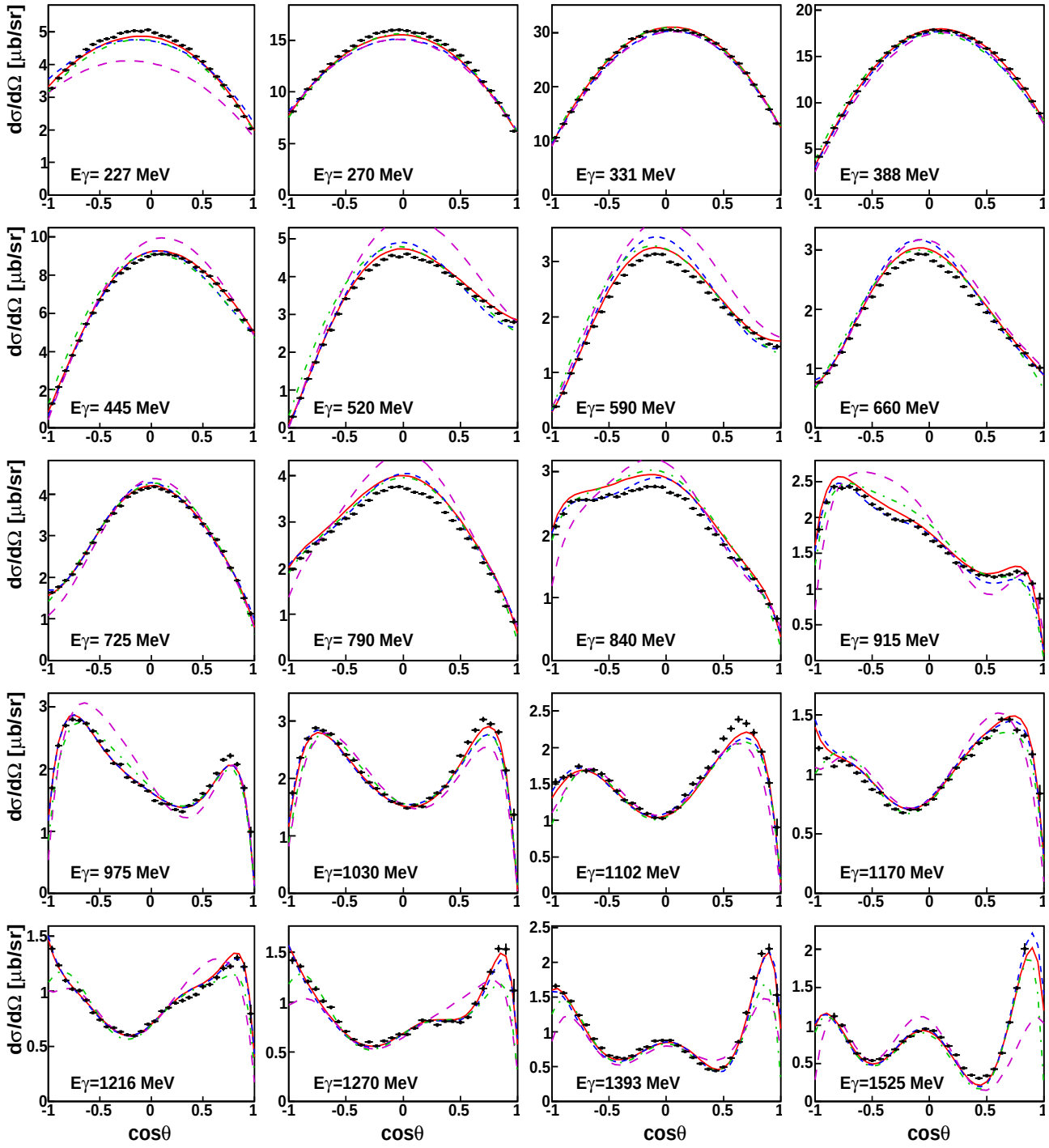

FIG. 7: (Color online) Selected results of this work (black points) for the $\gamma p \to \pi^0 p$ differential cross sections compared to existing PWA solutions from SAID CM12 [24] (blue dashed line), MAID2007 [30] (magenta long-dashed line), and Bonn-Gatchina BG2014-02 [31] (green dash-dotted line) and to a new SAID PR15 solution (red solid line) obtained after adding the present data points into the fit. The error bars on all data points represent statistical uncertainties only.

are plotted as a function of E_γ in Fig. 8(a) for the previous SAID solution DU13 [5] and for the new SAID PR15 solution, obtained after adding the present data into the fit. This comparison demonstrates the energies at which the new data give the most significant impact. The results obtained for the normalization parameter X from the DU13 and PR15 solutions are plotted as a function of E_γ in Fig. 8(b).

Another useful presentation of the new $\gamma p \to \pi^0 p$ results is obtained by plotting them as an excitation function at a particular production angle θ of π^0. In Fig. 9, the differential cross sections are shown as a function of

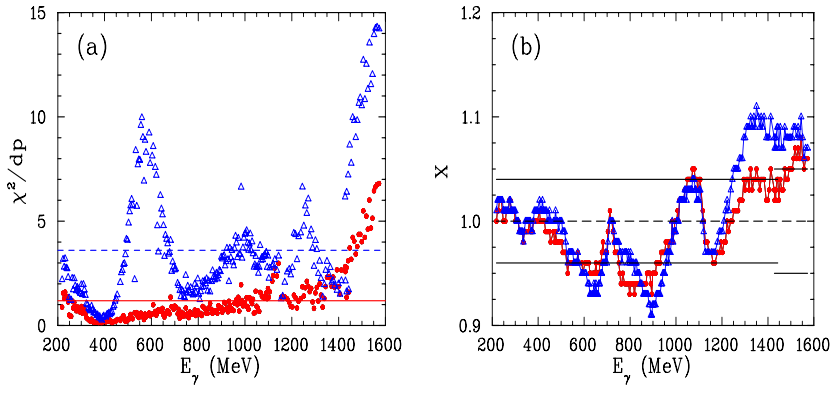

FIG. 8: (Color online) Comparison of the previous SAID solution DU13 [5] (blue open triangles) applied to the present data and the new SAID PR15 solution (red full circles) obtained after adding the present data into the fit for: (a) χ^2/dp values averaged only within each energy bin E_γ, where the horizontal lines (blue dashed for DU13 and red solid for PR15) show the corresponding χ^2/dp values from Table I; (b) results for the normalization parameter X as a function of E_γ, where the horizontal solid lines show the deviations (from the dashed line at $X = 1$) equal to the magnitute of the overall systematic uncertainties, which are 4% and 5% for the data from Run-I and Run-II, respectively.

the c.m. energy W for ten of 30 measured $\cos\theta$ bins. As seen, the peaks corresponding to the first, the second, and the third resonance region are clearly evident in the excitation function for each π^0 production angle. The experimental distributions are also compared to the three previous PWA solutions (SAID CM12 [24], MAID2007 [30], and BG2014-02 [31]) and the new SAID PR15 solution. For a better comparison in the energy range away from the $\Delta(1232)3/2^+$ peak, all distributions are also plotted after rescaling by a factor 5. The comparison demonstrates that the largest discrepancies are seen for the very forward and backward production angles.

The strongest dip in the $\gamma p \to \pi^0 p$ excitation function is observed at very backward π^0 angles at the c.m. energies slightly below $W = 1.4$ GeV. An example of the $\gamma p \to \pi^0 p$ differential cross section near this dip (namely, at $W = 1380$ MeV) is shown in Fig 10(a). This effect, caused by the nearly complete cancellation between different contributions to the production cross section, is even better seen in the results of the new SAID PR15 solution, shown in Fig 10(b) by a blue solid line for $\cos\theta = -1$ (or $\theta = 180°$). It is interesting that a very similar cancellation in the very backward π^0 production angles was observed in the charge-exchange reaction $\pi^- p \to \pi^0 n$ at the same energy range. The SAID WI08 solution [33] (rescaled by a factor 10^{-3}) for $\pi^- p \to \pi^0 n$ at $\theta = 180°$ is plotted in Fig 10(b) by a red dashed line. In contrast, the $\gamma p \to \pi^+ n$ reaction, depicted for the SAID PR15 solution by a black dashed line, has no such feature. Unfortunately, the quality and the angular coverage of the existing $\gamma n \to \pi^0 n$ data do not allow a reliable prediction for very backward production π^0 angles in this energy range [34].

For the c.m. energies above $W = 1.4$ GeV, the present results for very backward π^0 angles are in good agreement with similar results ($\theta = 170°$) published in Ref. [35], also showing a cusp structure at the η-photoproduction threshold ($W = 1.486$ GeV).

The statistical accuracy of the present results is sufficient for reliable fits of the $\gamma p \to \pi^0 p$ differential cross sections with series of Legendre polynomials up to a high order. Of course, such decompositions are much less reliable without full angular coverage of the π^0 production angle. Thus, the present results from Run-II should be used only in energy-dependent PWAs with additional model assumptions. For Run-I, we describe the $\gamma p \to \pi^0 p$ differential cross sections of each energy bin in terms of a series of orthogonal Legendre polynomials $P_j(\cos\theta)$:

$$\frac{d\sigma}{d\Omega}(W, \cos\theta) = \sum_{j=0}^{j_{\max}} A_j(W)\ P_j(\cos\theta),$$

with the energy-dependent decomposition coefficients $A_j(W)$.

From the phenomenological point of view, the number of terms required in the series, $j_{\max}$, is related to the angular momenta of essential partial-wave amplitudes or to the highest spin of resonances, existing in the studied energy range. An isolated resonance with spin $J = (2\ell + 1)/2$ can contribute to coefficients A_j only with even j up to $j = 2\ell$ and, hypothetically, to other coefficients via interference with sizable background amplitudes. For example, a wide four-star resonance $\Delta(2420)$ with $J^P = 11/2^+$ [6], although lying above the energy range of the present measurements, can affect A_j up to $j = 10$ by itself and even higher A_j via the interference with other states. On the other hand, the maximum order $j_{\max}$, up to which such a decomposition is meaningful, is limited by the data quality.

In this work, the data of Run-I were fitted up to order $j_{\max} = 10$. It was observed that including Legendre polynomials beyond $j_{\max} = 8$ in the fits could not significantly improve the reduced χ^2 (i.e., divided by the number of degrees of freedom, χ^2/ndf). The comparison of the reduced χ^2 for the fits of the data from Run-I with $j_{\max} = 6$, 8 and 10 is shown in Fig. 11, using only the statistical uncertainties. In the energy range around the $\Delta(1232)3/2^+$ region, which is below $W = 1.3$ GeV, fitting with $j_{\max} = 6$ should, in principle, be sufficient for a fairly good description of the differential cross sections. However, the high statistical accuracy, which arises from the very large cross sections, results in the reduced χ^2

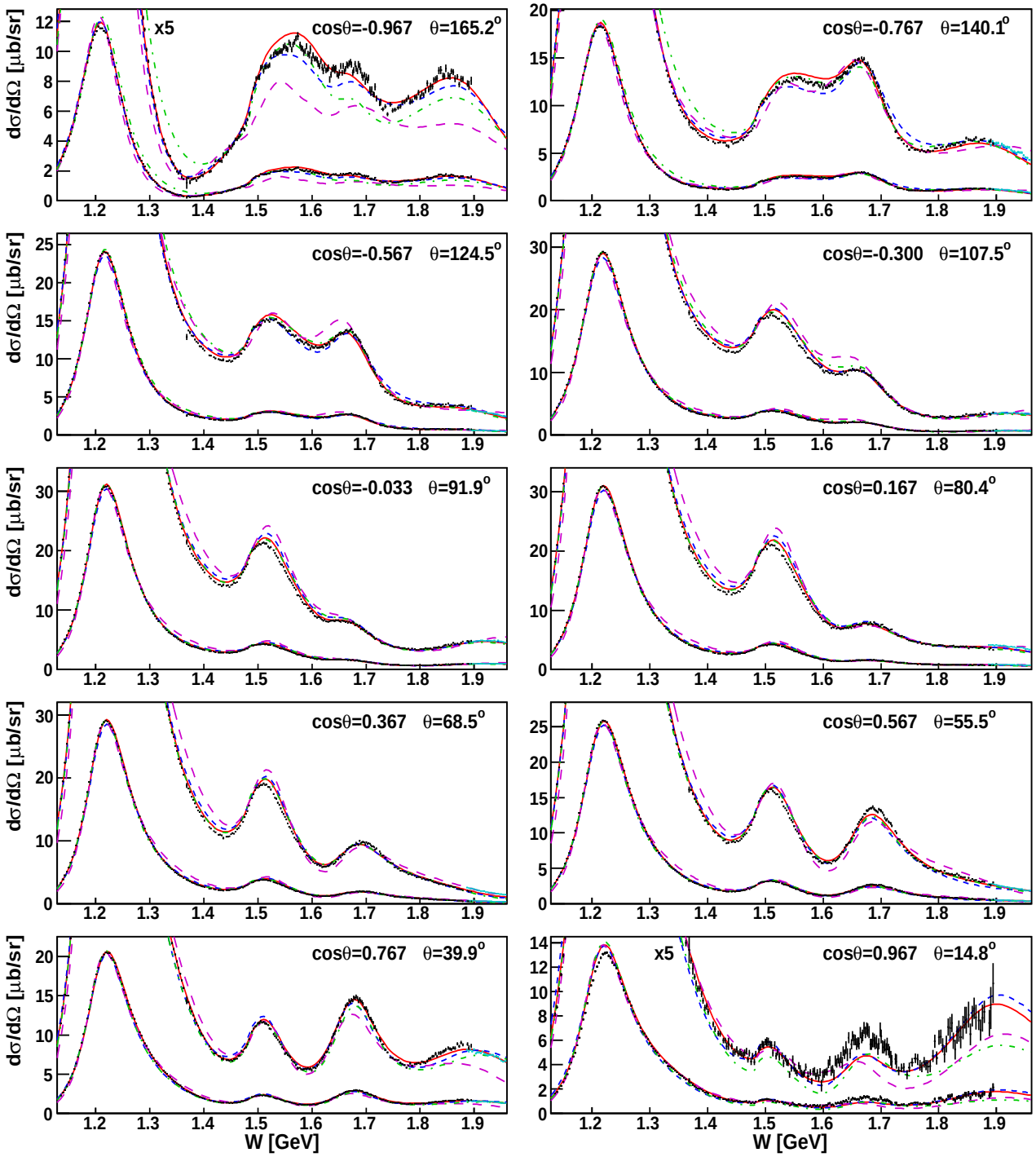

FIG. 9: (Color online) Present results for the $\gamma p \to \pi^0 p$ excitation function as a function of the c.m. energy W, shown for ten of 30 measured $\cos\theta$ bins (where θ is the π^0 production angle), are compared to previous PWA solutions from SAID CM12 [24] (blue dashed line), MAID2007 [30] (magenta long-dashed line), and BG2014-02 [31] (green dash-dotted line) and to a new SAID PR15 solution (red solid line). The error bars on all data points (black points for Run-I and cyan points for Run-II) represent statistical uncertainties only. For a better comparison, all distributions are also plotted after rescaling by a factor 5.

values varying mostly between two and three. As also seen in Fig. 11, including higher-order coefficients in the fits does not improve the situation much. It is necessary to take into account angular-dependent systematic uncertainties, with values varying between 1% and 2%, in order to obtain reasonable χ^2 values in the $\Delta(1232)3/2^+$ region, even in the fits with $j_{\max} = 6$. Above $W = 1.7$ GeV, using $j_{\max} = 6$ is not sufficient, and the data require the minimum order of $j_{\max} = 8$, corresponding to G-wave amplitudes.

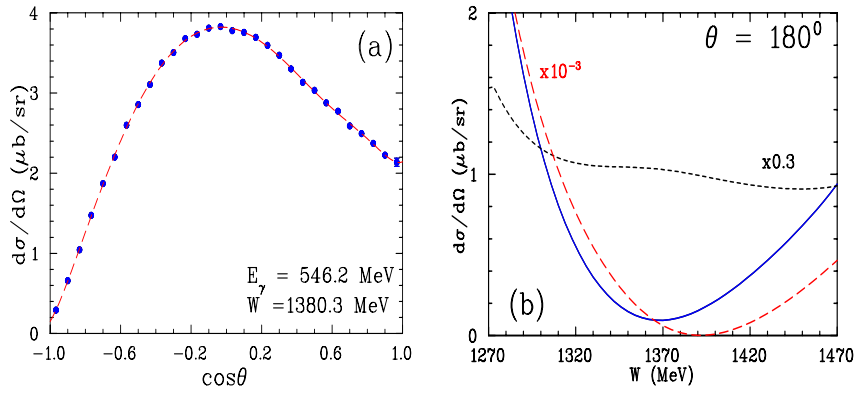

FIG. 10: (Color online) (a) present results for the $\gamma p \to \pi^0 p$ differential cross section (blue full circles) at E_γ = 546 MeV (W = 1380 MeV) fitted with Legendre polynomials (red dashed line); (b) the new SAID PR15 solution (blue solid line) for π^0 production angle θ = 180° ($\cos\theta = -1$) as a function of the c.m. energy W, compared with a similar $\pi^- p \to \pi^0 n$ prediction (rescaled by a factor 10^{-3}) from SAID WI08 [33] (red dashed line) and a $\gamma p \to \pi^+ n$ prediction (rescaled by a factor 0.3) from SAID PR15 (black dashed line).

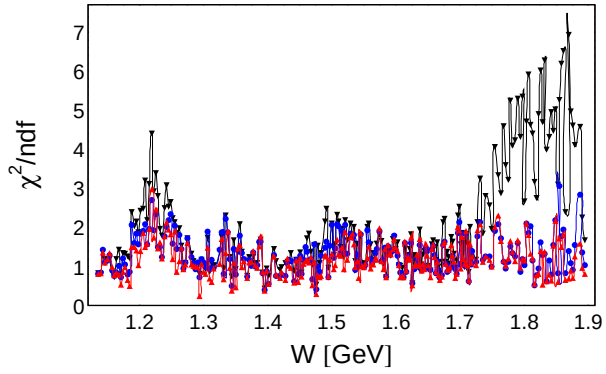

FIG. 11: (Color online) Energy dependence of the reduced χ^2 values for Legendre fits of the present $\gamma p \to \pi^0 p$ differential cross sections with $j_{\max} = 6$ (black triangles down), 8 (blue circles), and 10 (red triangles up), where the angular-dependent systematic uncertainties were not taken into account.

The results of the Legendre-polynomial fits for each coefficient A_j are depicted in Fig. 12, showing their energy dependence in unprecedented resolution. The A_j error bars represent uncertainties obtained from fits that took into account only the statistical uncertainties in the cross sections. As previously discussed, the effect from the angular-dependent systematic uncertainties should be considered, especially for the $\Delta(1232)3/2^+$ energy region. To estimate the impact from these uncertainties, the values of the differential cross section for each angular bin were randomly shifted within the uncertainty magnitude (2%), followed by a new Legendre-polynomial fit. Such a procedure was then repeated several times, and the average spread of the fit results for each A_j was considered as its systematic uncertainty caused by the angular-dependent systematic uncertainties in the differential cross sections. The systematic uncertainties in A_j, obtained from the fits with $j_{\max} = 10$, are depicted by a black histogram at the bottom of each plot in Fig. 12, clearly peaking at the position of $\Delta(1232)3/2^+$. In this region, the magnitudes of the systematic uncertainties in A_j at high orders are very close to the magnitudes of A_j themselves. The Legendre-polynomial fits for the c.m. energies below $W = 1280$ MeV were made for both $j_{\max} = 6$ and $j_{\max} = 10$. Their comparison showed good agreement of the results for A_0 to A_6.

One of the most obvious features in the energy dependence of A_j is the absence of any well-defined sharp structures, which could be associated with unknown narrow resonances. The results for A_0 show good agreement with the values for the total cross sections obtained by the integration of the differential cross sections, providing another confirmation of the good quality of the present data. The A_0 energy dependence clearly demonstrates the first, second, and third resonance regions, but appears structureless at higher energies. In contrast, some of the other A_j reveal structures even at the energies above the third resonance region. These structures could be associated with contributions from N^* and/or Δ^* states, with spins up to 7/2 or higher, that are known in this region or near it [6]. These resonances have masses close to the upper end of the studied energy range, as $\Delta(1950)7/2^+$, or even above it, as $N(2190)7/2^-$, $N(2220)9/2^+$, and $N(2250)9/2^-$, but their large widths ($\sim$ 300 MeV or even larger) make those resonance contributions noticeable in the present data.

In Fig. 12, the coefficients A_j are also compared to results obtained from the predictions generated with SAID CM12 [24], MAID2007 [30], BG2014-02 [31], and SAID PR15, by fitting them, after adding small uncertainties, with Legendre polynomials up to $j_{\max} = 10$. As seen, the Legendre-polynomial fits to the predictions of all models reproduce fairly well only the coefficients A_0 and A_2. Partial agreement is observed for A_1 and the coefficients A_3 to A_7. The coefficients A_8 to A_{10} are small and show some meaningful structures only above $W = 1.7$ GeV.

Of course, such a Legendre decomposition of the present differential cross sections is only a very first step towards a full single-energy partial-wave analysis. A direct extraction of partial-wave amplitudes by simultaneous fitting the present differential cross sections and polarization observables will be performed in the future. However, the present analysis already shows the sensitivity of the new data to partial-wave amplitudes up to G-waves ($\ell = 4$).

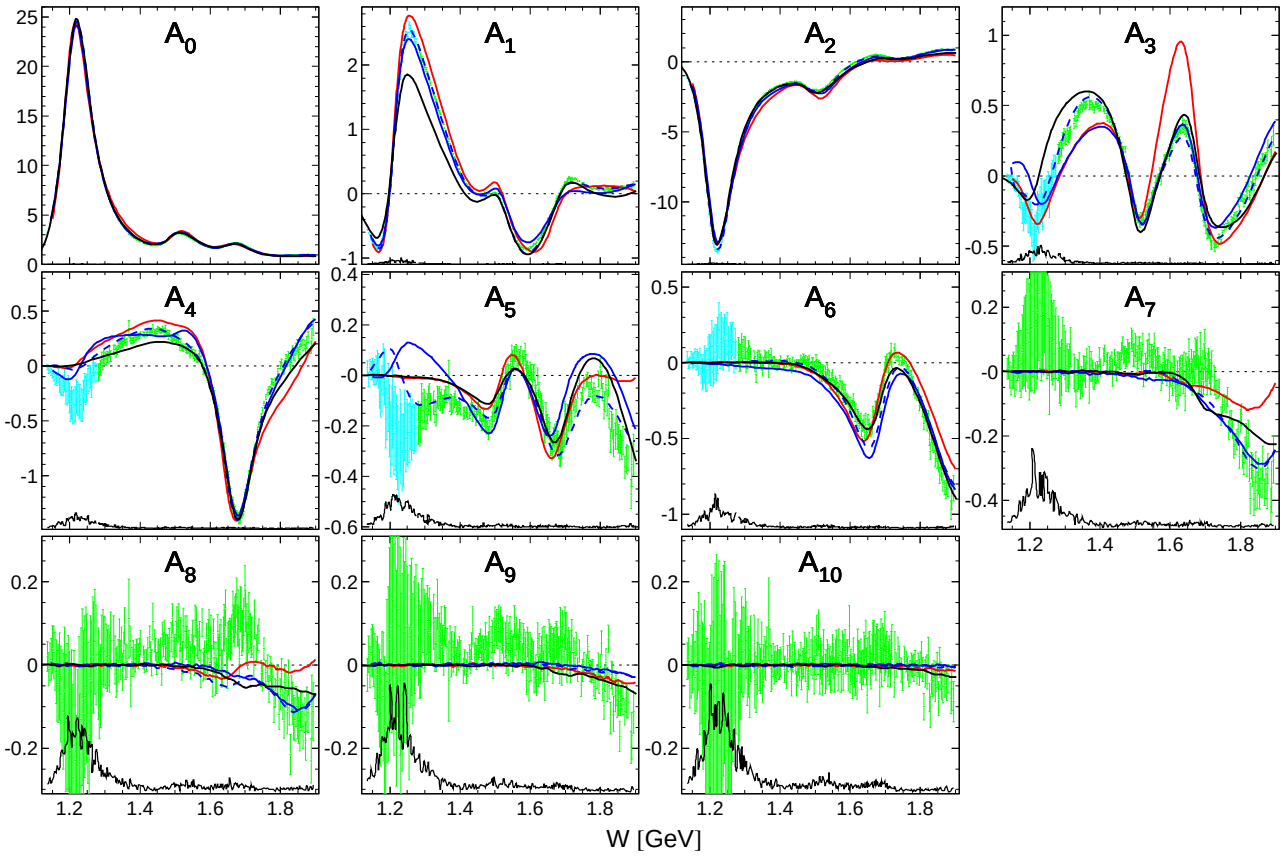

FIG. 12: (Color online) Coefficients A_j (in μb/sr units) obtained from fitting the present $\gamma p \to \pi^0 p$ differential cross sections with Legendre polynomials up to order six (cyan points) and ten (green points), compared to the results of the Legendre-polynomial fits ($j_{\max} = 10$) made to the predictions generated from SAID CM12 [24] (blue solid line), MAID2007 [30] (red solid line), BG2014-02 [31] (black solid line), and SAID PR15 (blue dashed line). The error bars on all points represent A_j uncertainties from the fits with using only the statistical uncertainties. A black histogram at the bottom of each plot shows the systematic uncertainty in A_j caused by the angular-dependent systematics in the differential cross sections.

V. SUMMARY AND CONCLUSIONS

New measurements of π^0 photoproduction on the proton have been conducted with the A2 tagged-photon facilities at energies provided by the Mainz Microtron, MAMI C, with a maximum electron-beam energy of 1.6 GeV. The differential cross sections, obtained with a fine energy and angular binning, increase the existing quantity of π^0 photoproduction data by $\sim 47\%$. A new solution PR15 of the SAID partial-wave analysis obtained after adding the new data into the fit is presented. The magnitudes of χ^2/dp obtained for this solution indicate that the new $\gamma p \to \pi^0 p$ data are consistent with the existing $\gamma N \to \pi N$ data sets. Owing to the unprecedented statistical accuracy and the full angular coverage, the results are sensitive to high partial-wave amplitudes. This is demonstrated by the decomposition of the differential cross sections in terms of Legendre polynomials and by further comparison to model predictions. The present data are expected to be invaluable for future partial-wave and coupled-channel analyses, which could provide much stronger constraints on the properties of nucleon states known in this energy range and, perhaps, even reveal new resonances. A more detailed analysis of the present $\gamma p \to \pi^0 p$ differential cross sections, combined with results from the A2 Collaboration obtained by measuring polarization observables, is currently in progress and will be published separately.

Acknowledgments

We thank A. Donnachie for useful remarks and continuous interest in the paper. The authors wish to acknowledge the excellent support of the accelerator group and operators of MAMI. This work was supported by the Deutsche Forschungsgemeinschaft (SFB443, SFB/TR16, and SFB1044), the European Community-Research Infrastructure Activity under the FP6 "Structuring the European Research Area" programme (Hadron Physics, Contract No. RII3-CT-2004-506078), Schweizerischer Nationalfonds (Contract No. 200020-156983, 132799, 121781, 117601, 113511), the UK Science and Technology Facilities Council (STFC 57071/1, 50727/1), the U.S. Department of Energy (Offices of Science and Nuclear Physics, Award Numbers DE-FG02-99-ER41110,

DE-FG02-88ER40415, DE-FG02-01-ER41194) and National Science Foundation (Grant No. PHY-1039130, IIA-1358175), INFN (Italy), and NSERC (Canada). Ya. I. Azimov acknowledges support by the Russian Science Foundation (Grant No. 14-22-00281). A. Fix acknowledges additional support from the TPU (Grant No. LRU-FTI-123-2014) and the MSE Program "Nauka" (Project No. 3.825.2014/K). We thank the undergraduate students of Mount Allison University and The George Washington University for their assistance.

[1] J. Steinberger, W. K. H. Panofsky, and J. Steller, Phys. Rev. **78**, 802 (1950); A. Silverman and M. Stearns, Phys. Rev. **83**, 853 (1951); W. K. H.Panofsky, J. Steinberger, and J. Steller, Phys. Rev. **86**, 180 (1952); A. Silverman and M. Stearnst, Phys. Rev. **88**, 1225 (1952); G. Cocconi and A. Silverman, Phys. Rev. **88**, 1230 (1952).
[2] E. M. McMillan, J. M. Peterson and R. S. White, Science **110**, 579 (1949); J. Steinberger and A. S. Bishop, Phys. Rev. **78**, 493 (1950); J. Steinberger and A. S. Bishop, Phys. Rev. **78**, 494 (1950); A. S. Bishop, J. Steinberger, and L. J. Coom, Phys. Rev. **80**, 291 (1950); J. Steinberger and A. S. Bishop, Phys. Rev. **86**, 171 (1952).
[3] R. S. White, M. J. Jacobson, and A. G. Schulz, Phys. Rev. **88**, 836 (1952).
[4] H. L. Anderson, E. Fermi, R. Martin, and D. E. Nagle, Phys. Rev. **91**, 155 (1953).
[5] M. Dugger *et al.*, Phys. Rev. C **88**, 065203 (2013).
[6] K. A. Olive *et al.*, (Particle Data Group), Chin. Phys. C **38**, 090001 (2014).
[7] O. Bartalini *et al.*, Eur. Phys. J. A **26**, 399 (2005).
[8] A. Thiel *et al.*, Phys. Rev. Lett. **109**, 102001 (2012).
[9] J. Hartmann *et al.*, Phys. Rev. Lett. **113**, 062001 (2014).
[10] M. Gottschall *et al.*, Phys. Rev. Lett. **112**, 012003 (2014).
[11] M. H. Sikora **et al.**, Phys. Rev. Lett. **112**, 022501 (2014).
[12] A. Starostin *et al.*, Phys. Rev. C **64**, 055205 (2001).
[13] R. Novotny, IEEE Trans. Nucl. Sci. **38**, 379 (1991).
[14] A. R. Gabler *et al.*, Nucl. Instrum. Methods A **346**, 168 (1994).
[15] H. Herminghaus *et al.*, IEEE Trans. Nucl. Sci. **30**, 3274 (1983).
[16] K.-H. Kaiser *et al.*, Nucl. Instrum. Methods A **593**, 159 (2008).
[17] S. Prakhov *et al.*, Phys. Rev. C **79**, 035204 (2009).
[18] I. Anthony *et al.*, Nucl. Instrum. Methods A **310**, 230 (1991).
[19] S. J. Hall *et al.*, Nucl. Instrum. Methods A **368**, 698 (1996).
[20] J. C. McGeorge *et al.*, Eur. Phys. J. A **37**, 129 (2008).
[21] A. Nikolaev *et al.*, Eur. Phys. J. A **50**, 58 (2014).
[22] E. F. McNicoll *et al.*, Phys. Rev. C **82**, 035208 (2010).
[23] W. J. Briscoe, D. Schott, I. I. Strakovsky, and R. L. Workman, Institute of Nuclear Studies of The George Washington University Database: http://gwdac.phys.gwu.edu/analysis/pr_analysis.html .
[24] R. L. Workman, M. W. Paris, W. J. Briscoe, and I. I. Strakovsky, Phys. Rev. C **86**, 015202 (2012).
[25] D. Hornidge *et al.*, Phys. Rev. Lett. **111**, 062004 (2013).
[26] R. Beck, R. Leukel and A. Schmidt, Acta Phys. Pol. B **33**, 813 (2002); R. Beck, Eur. Phys. J. A **28**, s01, 173 (2006).
[27] M. Dugger *et al.*, Phys. Rev. C **76**, 025211 (2007).
[28] O. Bartholomy *et al.*, Phys. Rev. Lett. **94**, 012003 (2005); H. van Pee **et al.**, Eur. Phys. J. A **31**, 61 (2007).
[29] V. Crede *et al.*, Phys. Rev. C **84**, 055203 (2011).
[30] The MAID analyses are available through the Mainz website: http://wwwkph.kph.uni-mainz.de/MAID/. See also D. Drechsel, S. S. Kamalov, and L. Tiator, Eur. Phys. J. A **34**, 69 (2007).
[31] The Bonn-Gatchina analyses are available through the Bonn website: http://pwa.hiskp.uni-bonn.de/. See also E. Gutz *et al.*, Eur. Phys. J. A **50**, 74 (2014).
[32] R. A. Arndt, W. J. Briscoe, I. I. Strakovsky, and R. L. Workman, Phys. Rev. C **66**, 055213 (2002).
[33] R. L. Workman, R. A. Arndt, W. J. Briscoe, M. W. Paris, and I. I. Strakovsky, Phys. Rev. C **86**, 035202 (2012).
[34] M. Dieterle *et al.*, Phys. Rev. Lett. **112**, 142001 (2014)
[35] K. H. Althoff *et al.*, Z. Physik C, Particles and Fields **1**, 327 (1979).